A quantum magnetic analogue to the critical point of water

https://doi.org/10.1038/s41586-021-03411-8

Received: 30 September 2020

Accepted: 26 February 2021

Published online: 14 April 2021

Check for updates

J. Larrea Jiménez[1,2], S. P. G. Crone[3,4], E. Fogh[2], M. E. Zayed[5], R. Lortz[6], E. Pomjakushina[7], K. Conder[7], A. M. Läuchli[8], L. Weber[9], S. Wessel[9], A. Honecker[10], B. Normand[2,11], Ch. Rüegg[2,11,12,13], P. Corboz[3,4], H. M. Rønnow[2]✉ & F. Mila[2]

At the liquid–gas phase transition in water, the density has a discontinuity at atmospheric pressure; however, the line of these first-order transitions defined by increasing the applied pressure terminates at the critical point[1], a concept ubiquitous in statistical thermodynamics[2]. In correlated quantum materials, it was predicted[3] and then confirmed experimentally[4,5] that a critical point terminates the line of Mott metal–insulator transitions, which are also first-order with a discontinuous charge carrier density. In quantum spin systems, continuous quantum phase transitions[6] have been controlled by pressure[7,8], applied magnetic field[9,10] and disorder[11], but discontinuous quantum phase transitions have received less attention. The geometrically frustrated quantum antiferromagnet $SrCu_2(BO_3)_2$ constitutes a near-exact realization of the paradigmatic Shastry–Sutherland model[12–14] and displays exotic phenomena including magnetization plateaus[15], low-lying bound-state excitations[16], anomalous thermodynamics[17] and discontinuous quantum phase transitions[18,19]. Here we control both the pressure and the magnetic field applied to $SrCu_2(BO_3)_2$ to provide evidence of critical-point physics in a pure spin system. We use high-precision specific-heat measurements to demonstrate that, as in water, the pressure–temperature phase diagram has a first-order transition line that separates phases with different local magnetic energy densities, and that terminates at an Ising critical point. We provide a quantitative explanation of our data using recently developed finite-temperature tensor-network methods[17,20–22]. These results further our understanding of first-order quantum phase transitions in quantum magnetism, with potential applications in materials where anisotropic spin interactions produce the topological properties[23,24] that are useful for spintronic applications.

In the pressure–temperature (P, T) phase diagram of water (Fig. 1a)[25,26], the line of first-order transitions terminates at $P_c = 221$ bar and $T_c = 374$ °C, defining the critical point where liquid and vapour become a single phase[1]. Although the first-order line has no critical scaling properties, its termination point does[2]. In the supercritical regime, around and above the critical point, there is no transition and indeed one may proceed continuously from liquid to vapour without ever undergoing one. Because their difference is defined not by a change in symmetry but by a scalar, the particle density, which can take two values at the discontinuity, the critical point is in the Ising universality class.

Quantum systems with only spin degrees of freedom enable theorists to realize entangled quantum many-body models, including those with exact solutions or ground states, and experimentalists to probe their properties on truly macroscopic lengthscales. An example of a two-dimensional (2D) quantum spin system that hosts a first-order quantum phase transition (QPT) between two exactly known ground states is provided by the $S = 1/2$ Heisenberg model in a fully frustrated bilayer geometry. In that system, it was shown theoretically[27] that the line of first-order transitions extending to finite temperatures is again terminated by an Ising critical point, as we summarize in the Methods section.

A quantum magnetic material with a related geometry, $SrCu_2(BO_3)_2$ (ref. [28]), has drawn intensive interest because of the extreme frustration of its orthogonal-dimer structure (Fig. 1b, inset). This realizes a $S = 1/2$ Heisenberg model formulated by Shastry and Sutherland[12] because of its exact ground state, a product of dimer singlets, at all small and intermediate values of the inter- to intra-dimer interaction ratios ($J/J_D < 0.675$)[14]. Although the frustration is manifest in many unusual

[1]Laboratory for Quantum Matter under Extreme Conditions, Institute of Physics, University of São Paulo, São Paulo, Brazil. [2]Institute of Physics, Ecole Polytechnique Fédérale de Lausanne (EPFL), Lausanne, Switzerland. [3]Institute for Theoretical Physics, University of Amsterdam, Amsterdam, The Netherlands. [4]Delta Institute for Theoretical Physics, University of Amsterdam, Amsterdam, The Netherlands. [5]Department of Physics, Carnegie Mellon University in Qatar, Doha, Qatar. [6]Department of Physics, Hong Kong University of Science and Technology, Kowloon, Hong Kong. [7]Laboratory for Multiscale Materials Experiments, Paul Scherrer Institute, Villigen-PSI, Switzerland. [8]Institut für Theoretische Physik, Universität Innsbruck, Innsbruck, Austria. [9]Institut für Theoretische Festkörperphysik, RWTH Aachen University, Aachen, Germany. [10]Laboratoire de Physique Théorique et Modélisation, CNRS UMR 8089, CY Cergy Paris Université, Cergy-Pontoise, France. [11]Paul Scherrer Institute, Villigen-PSI, Switzerland. [12]Institute for Quantum Electronics, ETH Zürich, Hönggerberg, Switzerland. [13]Department of Quantum Matter Physics, University of Geneva, Geneva, Switzerland. ✉e-mail: henrik.ronnow@epfl.ch

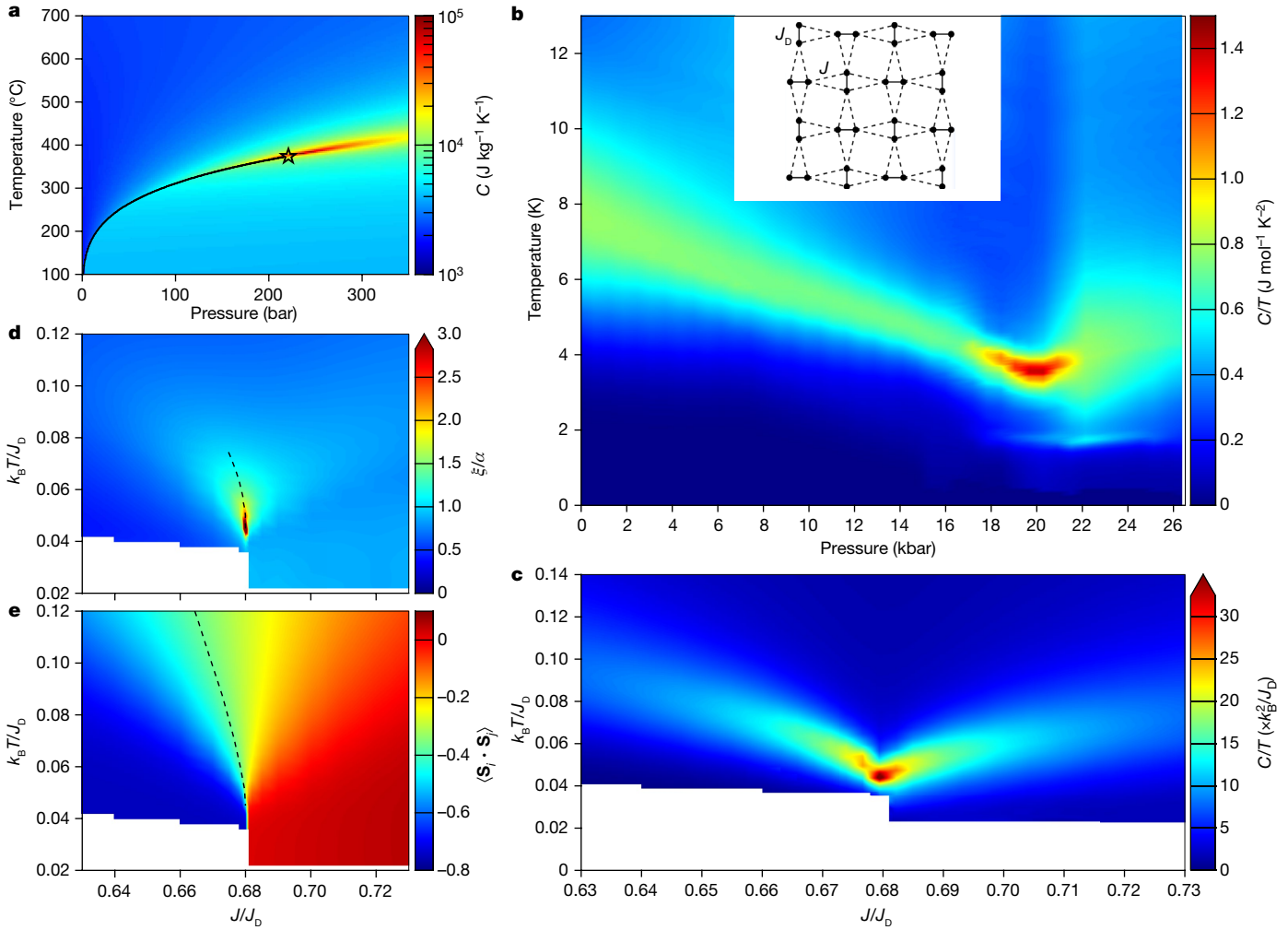

Fig. 1 | Specific heat of water and of $SrCu_2(BO_3)_2$, shown together with calculated critical properties of the Shastry–Sutherland model. a, Specific heat of water, $C(P, T)$, shown as a function of pressure and temperature. The black line marks the first-order phase boundary separating liquid (lower left) from vapour (upper left) and the black star marks the critical point. **b**, Experimental data for the specific heat, $C(P, T)/T$, of $SrCu_2(BO_3)_2$. Below 18 kbar is the dimer product phase and above 20 kbar is the plaquette phase. The two lines of maxima meet at the critical point at approximately 19 kbar and 3.3 K. The inset shows the orthogonal-dimer geometry of the Shastry–Sutherland model, which is realized by the Cu^{2+} ions ($S = 1/2$) in $SrCu_2(BO_3)_2$. **c**, Specific heat obtained by iPEPS calculations with $D = 20$ performed for the Shastry–Sutherland model with different values of the coupling ratio, J/J_D, which in $SrCu_2(BO_3)_2$ was shown to be an approximately linear function of the applied pressure[18]. **d**, Correlation length, ξ, obtained by iPEPS with $D = 20$ and expressed in units of the lattice constant, a. ξ becomes large only at the finite-temperature critical point; the dashed black line shows the locus of maxima of $\xi(J/J_D)$ at each fixed temperature, and terminates when $\xi/a < 1$. We note that the colour scales in **c** and **d** are truncated such that they do not include the peak values of C/T and ξ. **e**, Dimer spin–spin correlation function, $\langle \mathbf{S}_i \cdot \mathbf{S}_j \rangle$, showing a discontinuity with J/J_D at low temperatures but continuous behaviour throughout the supercritical regime. The dashed black line, the equivalent of the critical isochore in water, shows the locus of points where this order parameter is constant at its critical-point value, $\langle \mathbf{S}_i \cdot \mathbf{S}_j \rangle = -0.372(30)$.

phenomena[15–17], our interest in the Shastry–Sutherland model lies first in the presence of two first-order QPTs, from the dimer phase to a plaquette phase at $J/J_D = 0.675(2)$ and thence to an ordered Néel antiferromagnet at $J/J_D = 0.765(15)$[14], and second in the fact that applying a hydrostatic pressure to $SrCu_2(BO_3)_2$ acts to control J/J_D, revealing both transitions at respective pressures of approximately 19 kbar (ref. [18]) and 27 kbar (ref. [19]).

To investigate the possibility of a critical point in $SrCu_2(BO_3)_2$, we perform high-precision measurements of the specific heat using an a.c. calorimetry technique[29]. Large single crystals of $SrCu_2(BO_3)_2$ were grown by a floating-zone method (Methods). Samples of masses up to 36 mg were cut, patterned with metallic strips for calorimetry and mounted in a clamp cell allowing hydrostatic pressures up to 26.5 kbar and in applied magnetic fields up to 9 T. Details of our a.c. measurement procedures are provided in Methods and Extended Data Fig. 1.

Results: zero field

Starting at zero magnetic field, the pressure-induced evolution of the specific heat, shown as $C(T)/T$, is illustrated in Fig. 1b. As quantified in Fig. 2a, $C(T)/T$ at low pressures shows an exponential rise to a broad maximum at a temperature, T_{max}, that tracks the gap to the triplon or bound-triplon excitations of the dimer phase[17]. With increasing P, this peak moves gradually lower and becomes proportionately narrower, but between 18 and 20 kbar it becomes extremely tall and narrow (Figs. 1b, 2a), bearing all the characteristics of a critical point. After reaching a lowest measured value of 3.4 K at $P = 20$ kbar, T_{max} rises with increasing pressure and the peak broadens again (Fig. 2b), indicating that the singular behaviour has terminated. A second small peak appears around 2 K for $P \geq 18$ kbar (Figs. 1b, 2a, b) and persists to our upper pressure limit. We expect that this feature marks the thermal transition out of the plaquette phase

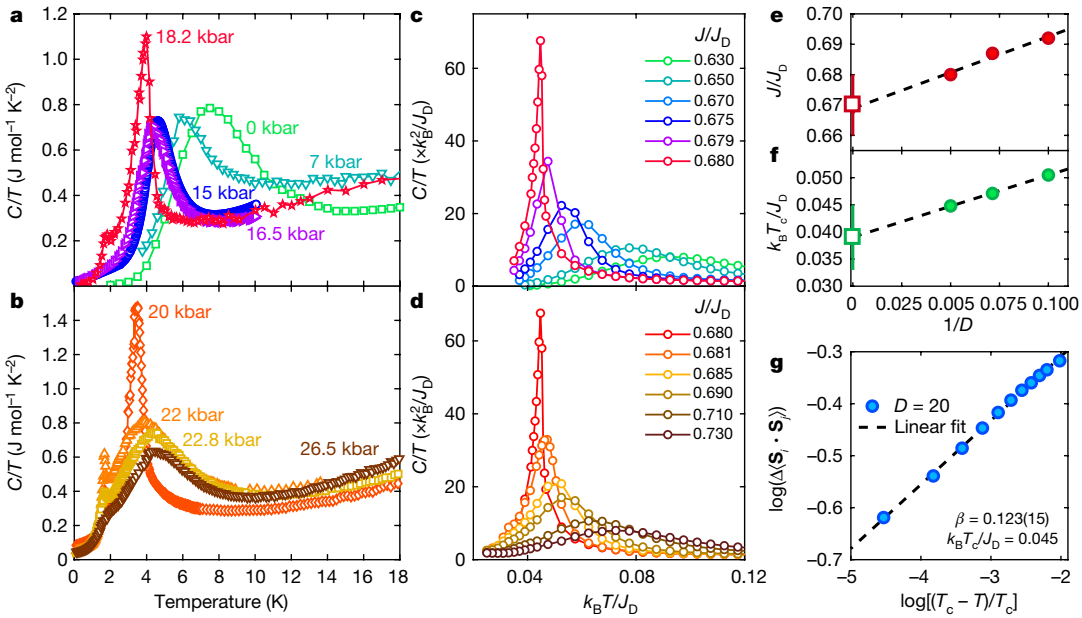

Fig. 2 | Specific heat and critical scaling at zero magnetic field. a, **b**, $C(T)/T$ measured for applied pressures from 0 to 18.2 kbar (**a**) and from 20 to 26.5 kbar (**b**). The temperature of the broad peak that is observed at most pressures ($P \leq 15$ kbar and $P \geq 22$ kbar) drops to a finite minimum value at the QPT, where $C(T)/T$ displays only a tall and extremely narrow peak. **c**, **d**, Specific heat obtained by $D = 20$ iPEPS calculations performed for the Shastry–Sutherland model in the dimer (**c**) and plaquette (**d**) phases using plaquette-based tensors (Methods). The evolution of peak heights with proximity to the critical coupling ratio, illustrated clearly in the numerical data, is less apparent in experiment. We note that the phonon contribution ($C(T)/T \propto T^2$) to the measured specific heat becomes appreciable at higher temperatures; although this can be subtracted for accurate fitting[17], our focus here is on the peak positions at and below 6 K. **e**, Convergence of the critical coupling ratio obtained in finite-temperature iPEPS calculations as a function of $1/D$ (solid circles); the extrapolated value of 0.67(1) (open square) agrees well with the zero-temperature value[14]. **f**, Convergence of the critical temperature as a function of $1/D$ (solid circles), leading to the estimate $k_B T_c/J_D = 0.039(6)$ (open square). The error bars on the extrapolated values (open squares) are conservative estimates based on their separation from the last calculated point. **g**, Critical exponent, $\beta = 0.123(15)$, of the discontinuity, $\Delta\langle \mathbf{S}_i \cdot \mathbf{S}_j \rangle$, in the dimer spin–spin correlation function at the first-order transition line, demonstrating consistency with the 2D Ising exponent, $\beta = 1/8$.

and remark that it seems to remain well below the 3.4 K peak at all pressures.

To model these thermodynamic results we use the method of infinite projected entangled pair states (iPEPS), which is a variational tensor-network ansatz for the representation of a quantum state on an infinite lattice[20,21]. The accuracy of the ansatz is controlled by the bond dimension, D, of the tensors (Methods). Whereas iPEPS has been applied previously to discuss the ground state of the Shastry–Sutherland model[14,15,30], here we apply recently developed methods[17,22] for representing the thermal states of the system. We analyse the pure Shastry–Sutherland model, by which is meant a single 2D layer (Fig. 1b, inset); $SrCu_2(BO_3)_2$ is known to have weak and frustrated interlayer interactions (at most 10% of J_D), Dzyaloshinskii–Moriya interactions (3%)[31] and higher-order further-neighbour interactions, none of which affect the first-order nature of the dimer–plaquette transition.

iPEPS results for $C(T)/T$ as a function of J/J_D, presented in Fig. 1c, show the same evolution as in $SrCu_2(BO_3)_2$ under pressure. The broad peaks of the gapped dimer and plaquette states move to lower temperatures on approaching the QPT and narrow to a tall, sharp spike at a critical coupling ratio (Fig. 2c, d). Figure 1d shows that the correlation length grows dramatically around this critical point, as Extended Data Fig. 2 also makes clear, but remains small at temperatures below it. Figure 1e illustrates how the average dimer spin–spin correlation, a scalar that serves as an order parameter for the nature of the spin state, has one discontinuous jump at all temperatures $T < T_c$, defining a clear line of first-order transitions, but changes to a smooth function of J/J_D at $T \geq T_c$, in direct analogy to the density of water molecules.

Our iPEPS results computed with $D = 10$, 14 and 20 show the same qualitative forms and provide good quantitative convergence (Fig. 2e, f) towards the critical coupling ratio of zero-temperature iPEPS[14]. From this we estimate the critical temperature $k_B T_c = 0.039(6) J_D$ (k_B, Boltzmann constant). We work in units of J_D because the exact P dependence of the magnetic interactions in $SrCu_2(BO_3)_2$ is subject to further uncertainty; taking a linear extrapolation at constant J, with errors provided by alternative estimates[18], a value $J_D(P_c)/k_B = 77(8)$ K gives a best estimate of $T_c = 3.0(6)$ K, in excellent agreement with experiment. By analysing the critical scaling of the discontinuity for $D = 20$, we deduce (Fig. 2g) that the exponent is fully consistent with the value $\beta = 1/8$ expected of a 2D Ising transition.

Turning to the line of thermal transitions appearing below the critical point in $SrCu_2(BO_3)_2$ (Fig. 1b), iPEPS calculations near the critical coupling become increasingly challenging at low temperatures (Methods). Although working with a finite Dzyaloshinskii–Moriya interaction allows access to lower temperatures on both sides of the discontinuity simultaneously, as we show in Extended Data Fig. 3, we are not currently able to obtain quantitatively reliable information about the thermal transitions of the plaquette phase.

Nevertheless, by combining our experimental and numerical results we now have enough information to answer the key question about the connection between the lines of thermal and first-order transitions. There are a priori two scenarios. (i) The first-order line terminates at an isolated critical point at $T = T_c$ and the thermal line ends when it meets the first-order line at an intermediate temperature, $T < T_c$, forming a separate 'critical endpoint'. (Note that, in statistical mechanics terminology[32,33], the termination of a line of first-order transitions is a 'critical point' and the term 'critical endpoint' is reserved for the termination of a line of continuous phase transitions[27].) (ii) The first-order line transforms into the (second-order) thermal line at a tricritical point. From experiment, the thermal line remains at a near-constant temperature close to 2 K and well below T_c (Figs. 1b, 2a, b). Numerically, we have

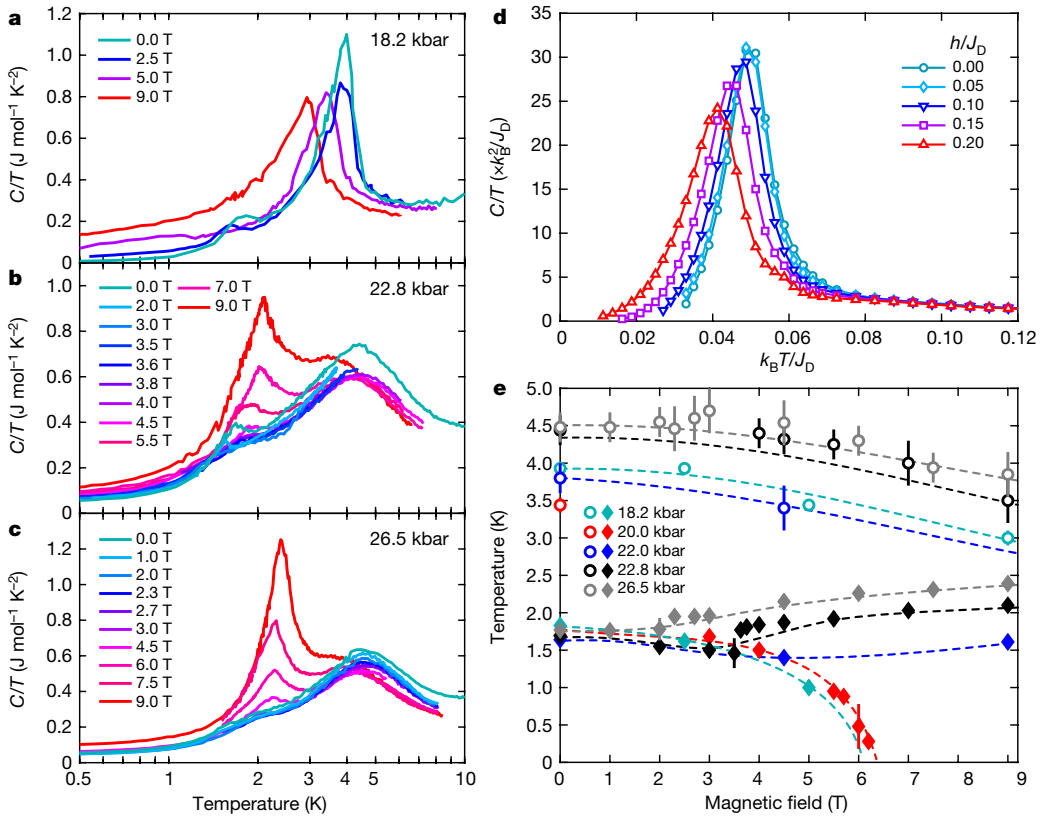

Fig. 3 | Evolution of the specific heat with magnetic field around the QPT. **a**, $C(T)/T$ at 18.2 kbar for four different applied fields up to $\mu_0 H = 9$ T. The peak due to the critical point retains its sharp nature and moves only slightly downwards in position and height with increasing field. **b**, $C(T)/T$ at 22.8 kbar for multiple different applied fields, showing initial field-induced suppression of the low-temperature transition followed by a dramatic change in shape to a sharp low-T peak with only a minimal hump at higher energies. **c**, $C(T)/T$ at 26.5 kbar, illustrating the field-induced emergence of the new, sharp peak at 9 T, the shape and size of which are suggestive of the transition to the antiferromagnetic phase. **d**, $C(T)/T$ computed by iPEPS at $J/J_D = 0.686$, close to the critical point for $D = 14$, for a range of applied magnetic fields. As in **a**, the sharp peak due to the critical point undergoes only a minor field-induced suppression of its position and height, and its width is unaltered. For the g factor of $SrCu_2(BO_3)_2$, a field $h/J_D \equiv g\mu_B\mu_0 H/J_D = 0.2$ (μ_B, Bohr magneton) corresponds to approximately 11 T. **e**, Characteristic field and temperature scales revealed by our full set of specific-heat measurements, which separate into high-T features (open symbols) around 4 K and low-T features (solid symbols) around and below 2 K. The high-T feature is the broad maximum, which at the critical point evolves into the sharp peak. The low-T feature at the lower pressures is the small peak due to the thermal Ising transition out of the plaquette phase, which can be suppressed to $T = 0$ by the applied field. At the higher pressures this feature changes into the strong peaks arising from the thermal transition of the antiferromagnetic phase, which is favoured by the applied field. Error bars represent uncertainties in the centres of particularly broad or anomalously shaped peaks.

identified an isolated critical point (Fig. 1e), with the Ising exponent $\beta = 1/8$ (Fig. 2g), in the Shastry–Sutherland model. Thus our results confirm scenario (i) and we place the critical point of $SrCu_2(BO_3)_2$ at $P_c \approx 19$ kbar and $T_c \approx 3.3$ K.

Results in a magnetic field

To challenge our interpretation, we consider the situation in a finite magnetic field. Because the field has little effect on the gapped dimer and plaquette phases, the physics of the critical point should be essentially unaffected. We have measured the specific heat in fields up to $\mu_0 H = 9$ T (μ_0, vacuum permeability; H, magnetic field strength), and indeed we observe near the critical point (18.2 kbar, Fig. 3a) that the peak remains sharp and shows only minor field-induced changes. These features are reproduced in detail by our iPEPS results, shown in Fig. 3d for a J/J_D value very close to the $D = 14$ QPT; the results also indicate that the small changes can result simply from not pinpointing the exact critical coupling.

Turning to the peak around 2 K, our 18.2-kbar and 22.8-kbar data (Fig. 3a, b) show that the field suppresses both its height and position. However, above 5.5 T for 22.8 kbar, another peak has emerged that is very different in shape, becoming tall, sharp and isolated from the broad 4-K hump, which has almost vanished above 4 T in our 26.5-kbar data (Fig. 3c). In Fig. 3e we collect all of these peaks to obtain a clear picture of three key phenomena. First, the 4-K features remain isolated, changing from sharp to broad with increasing P and H in a manner mostly independent of the complex action below 2.5 K. Second, the thermal transition of the plaquette phase is suppressed to zero temperature by fields of 6 T at 18.2 and 20.0 kbar; this field value is consistent with a closing of the gap to the triplet plaquette excitation observed in previous work[18]. Third, this suppression is replaced at our higher pressures and fields by the emergence at finite temperatures of the new, sharp peak, which from its field-induced evolution we attribute to the ordering transition of the antiferromagnetic phase.

We note that zero-field $C(T)$ data similar to ours have appeared recently[19]. These authors did observe the tall, sharp critical-point peak in their data at 19 and 21 kbar (1.9 and 2.1 GPa, shown only in their supplemental materials), but provided no explanation. They also observed the 2-K peak and ascribed it to a plaquette state (which they assume to be the 'empty' plaquette phase, see below), the deduced gap of which is also consistent with the 6-T critical field we observe. At pressures just beyond the limits of our study, they also argued that the pressure-induced development of the 2-K feature is a signature of the antiferromagnetic phase, and hence our observation of strong,

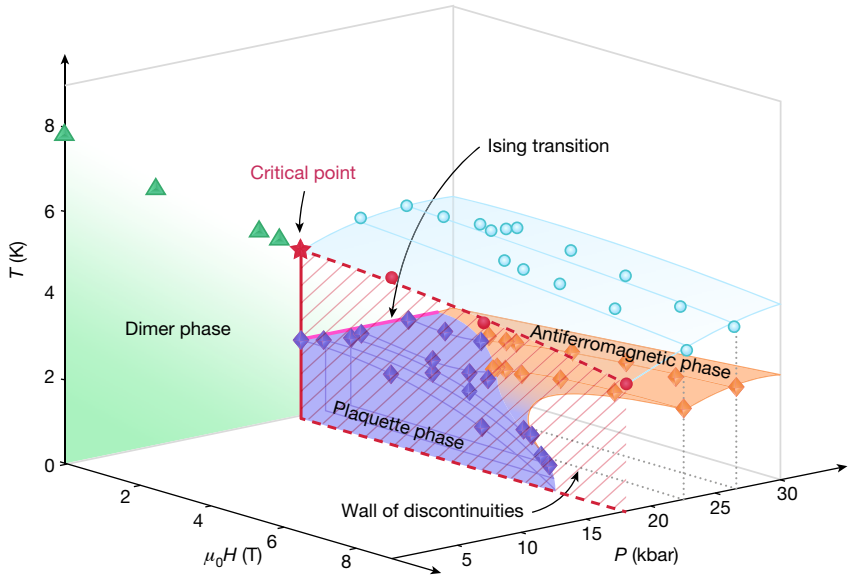

Fig. 4 | Phase diagram of $SrCu_2(BO_3)_2$ in pressure, field and temperature. The turquoise surface and green triangles indicate the locations of the maxima in $C(T)/T$ in the plaquette and dimer phases, respectively. These evolve into the critical point (red star, $T_c = 3.3$ K) in the (P, T) plane. The solid vertical red line below the critical point shows the location of the line of first-order discontinuities at $H = 0$; the thick dashed red lines and red grading mark the wall of discontinuities that extends to finite magnetic field and terminates at critical temperatures (red circles) that fall only slowly with H. The horizontal magenta line marks the measured location of the Ising transition out of the plaquette phase at $H = 0$. The blue surface marks the volume of parameter space occupied by the plaquette phase: its upper surface is the continuation of the magenta transition line to finite fields and at low pressures it is delimited by the wall of discontinuities. The orange colour indicates the surface of thermal transitions out of the antiferromagnetic phase. Purple and orange symbols mark specific-heat peaks measured on the respective surfaces.

sharp features in an applied field (Fig. 3b, c) helps to confirm their identification.

Phase diagram

In Fig. 4 we gather all the features abstracted from our specific-heat data as a function of both the applied magnetic field and the pressure. The (P, T) plane shows the critical point (red star) lying well above the line of thermal Ising transitions. On the scale of the figure, the first-order line is essentially vertical in temperature[27]. Although a structural transition is probably associated with the magnetic transition in $SrCu_2(BO_3)_2$, causing a discontinuity in the coupling constants, we stress that there is only one transition as a function of J/J_D (Fig. 1). This picture of the critical point at $H = 0$ is reinforced by the data at finite fields, which indicate a line of critical points, and a wall of first-order transitions, that dominate the (P, H, T) phase diagram. Below $T_c(P, H)$, this wall defines a plane through which the average dimer spin–spin correlation should change discontinuously, a prediction that may be tested by measuring the P dependence of the instantaneous spin correlation function by neutron scattering, or of phonon modes sensitive to the magnetic correlations[34].

At temperatures below the critical point in Fig. 4, our data reveal a wealth of quantum and thermal phase transitions. The field suppresses the continuous thermal transitions out of the plaquette phase and in its place we have found the antiferromagnetic phase at pressures as low as 22.8 kbar. The pressure-induced plaquette–antiferromagnetic QPT was thought to be weakly first-order[14], but has recently been proposed as a candidate deconfined quantum critical point[35]. Although our data suggest that the field-induced plaquette–antiferromagnetic QPT could change from first to second order between different regimes, there is no clear sign of another finite-temperature critical point. Establishing the universality classes of these transitions remains a challenge that is driving progress both in specific-heat measurements under extreme (P, H, T) conditions and in numerical methods for computing the thermal properties of frustrated systems.

Although our iPEPS studies of the Shastry–Sutherland model give a quantitative account of the critical-point physics of $SrCu_2(BO_3)_2$, they differ from experimental data on the nature of the plaquette-ordered phase. NMR[36] and neutron scattering experiments[18] indicate that in the plaquette phase of $SrCu_2(BO_3)_2$ the singlets form on the 'full' plaquettes of the J lattice (those with a J_D bond in the inset of Fig. 1b), whereas the Shastry–Sutherland model favours singlets on the 'empty' plaquettes. From the sensitive energetic competition between the empty-plaquette and full-plaquette phases[30], it is not surprising that the additional three-dimensional and Dzyaloshinskii–Moriya terms in $SrCu_2(BO_3)_2$ could cause this discrepancy, and we expect the state we observe above 18 kbar and below 2 K to be the full-plaquette phase. Because both plaquette phases have twofold degenerate ground states (only half of the plaquettes may form singlets), the thermal transition has Ising symmetry independent of their empty-plaquette or full-plaquette nature, and our results are not affected by this issue.

The physics of the critical-point phase diagram is different from that of second-order QPTs: because one may pass from one side of the discontinuity to the other without crossing a transition, there is no breaking of symmetry. At the critical point itself, the property of a divergent correlation length (Fig. 1d, Extended Data Fig. 2), associated with domain sizes and having critical exponents set by the universality class, remains. The supercritical regime has recently become a subject of active investigation, including (with a view to sensitive switching) in critical fluids[37]. In the Mott metal–insulator phase diagram, and its realization in the Hubbard model[38], theory[39,40] and experiment[41] have suggested the emergence of quantum critical scaling in this regime. In $SrCu_2(BO_3)_2$, the striking feature of the phase diagram is that the temperature, T_{max}, characterizing the peak in C/T reaches a minimum at T_c. We show in Extended Data Fig. 4 that this behaviour is universal around an Ising critical point in 2D lattice models. Thus the specific heat clearly defines not one but two characteristic lines in the supercritical regime (Fig. 1b, c), in contrast to the correlation length (Fig. 1d) and the critical isochore (Fig. 1e), both of which are regarded as marking a single crossover line.

Although this remarkable property of the specific heat is different from that in water (Fig. 1a), we stress that it is intrinsic to a system as simple as the Ising model. While the origin of this complex critical-point physics awaits further theoretical analysis, we observe that its consequences can be probed experimentally in quantum spin systems by comparing the specific heat with scattering measurements of the order parameter. As modern quantum magnetism and spintronics embrace the highly spin-anisotropic interactions required to produce the topological physics of Ising, Kitaev, skyrmion and other systems, a full understanding of the resulting first-order QPTs will include the quantum phenomenology of the critical point, the classical variant of which has been known to science for two centuries.

Online content

Any methods, additional references, Nature Research reporting summaries, source data, extended data, supplementary information, acknowledgements, peer review information; details of author contributions and competing interests; and statements of data and code availability are available at https://doi.org/10.1038/s41586-021-03411-8.

1. Cagniard de la Tour, C. Exposé de quelques résultats obtenus par l'action combinée de la chaleur et de la compression sur certains liquides, tels que l'eau, l'alcool, l'éther sulfurique et l'essence de pétrole rectifié. *Ann. Chim Phys*. **21**, 127–132 (1822).
2. Chaikin, P. M. & Lubensky, T. C. *Principles of Condensed Matter Physics* (Cambridge Univ. Press, 1995).
3. Georges, A., Kotliar, G., Krauth, W. & Rozenberg, M. J. Dynamical mean-field theory of strongly correlated fermion systems and the limit of infinite dimensions. *Rev. Mod. Phys*. **68**, 13–125 (1996).
4. Limelette, P. et al. Universality and critical behavior at the Mott transition. *Science* **302**, 89–92 (2003).
5. Kagawa, F., Miyagawa, K. & Kanoda, K. Unconventional critical behaviour in a quasi-two-dimensional organic conductor. *Nature* **436**, 534–537 (2005).
6. Sachdev, S. *Quantum Phase Transitions* (Cambridge Univ. Press, 2011).
7. Rüegg, C. et al. Quantum magnets under pressure: controlling elementary excitations in $TlCuCl_3$. *Phys. Rev. Lett*. **100**, 205701 (2008).
8. Merchant, P. et al. Quantum and classical criticality in a dimerized quantum antiferromagnet. *Nat. Phys*. **10**, 373–379 (2014).
9. Giamarchi, T., Rüegg, C. & Tchernyshyov, O. Bose–Einstein condensation in magnetic insulators. *Nat. Phys*. **4**, 198–204 (2008).
10. Thielemann, B. et al. Direct observation of magnon fractionalization in a quantum spin ladder. *Phys. Rev. Lett*. **102**, 107204 (2009).
11. Yu, R. et al. Bose glass and Mott glass of quasiparticles in a doped quantum magnet. *Nature* **489**, 379–384 (2012).
12. Shastry, B. S. & Sutherland, B. Exact ground state of a quantum mechanical antiferromagnet. *Physica B+C* **108**, 1069–1070 (1981).
13. Miyahara, S. & Ueda, K. Theory of the orthogonal dimer Heisenberg spin model for $SrCu_2(BO_3)_2$. *J. Phys. Condens. Matter* **15**, 327–366 (2003).
14. Corboz, P. & Mila, F. Tensor network study of the Shastry–Sutherland model in zero magnetic field. *Phys. Rev. B* **87**, 115144 (2013).
15. Matsuda, Y. H. et al. Magnetization of $SrCu_2(BO_3)_2$ in ultrahigh magnetic fields up to 118 T. *Phys. Rev. Lett*. **111**, 137204 (2013).
16. Knetter, C., Bühler, A., Müller-Hartmann, E. & Uhrig, G. S. Dispersion and symmetry of bound states in the Shastry–Sutherland model. *Phys. Rev. Lett*. **85**, 3958–3961 (2000).
17. Wietek, A. et al. Thermodynamic properties of the Shastry–Sutherland model throughout the dimer-product phase. *Phys. Rev. Res*. **1**, 033038 (2019).
18. Zayed, M. E. et al. 4-spin plaquette singlet state in the Shastry–Sutherland compound $SrCu_2(BO_3)_2$. *Nat. Phys*. **13**, 962–966 (2017).
19. Guo, J. et al. Quantum phases of $SrCu_2(BO_3)_2$ from high-pressure thermodynamics. *Phys. Rev. Lett*. **124**, 206602 (2020).
20. Verstraete, F. & Cirac, J. I. Renormalization algorithms for quantum-many body systems in two and higher dimensions. Preprint at https://arxiv.org/abs/cond-mat/0407066 (2004).
21. Jordan, J., Orús, R., Vidal, G., Verstraete, F. & Cirac, J. I. Classical simulation of infinite-size quantum lattice systems in two spatial dimensions. *Phys. Rev. Lett*. **101**, 250602 (2008).
22. Czarnik, P., Dziarmaga, J. & Corboz, P. Time evolution of an infinite projected entangled pair state: an efficient algorithm. *Phys. Rev. B* **99**, 035115 (2019).
23. Witczak-Krempa, W., Chen, G., Kim, Y.-B. & Balents, L. Correlated quantum phenomena in the strong spin–orbit regime. *Annu. Rev. Condens. Matter Phys*. **5**, 57–82 (2014).
24. Chacon, A. et al. Observation of two independent skyrmion phases in a chiral magnetic material. *Nat. Phys*. **14**, 936–941 (2018).
25. Wagner, W. et al. The IAPWS Industrial Formulation 1997 for the Thermodynamic Properties of Water and Steam. *J. Eng. Gas Turbine. Power* **122**, 150–184 (2000).
26. Orlov, K. A., Alexandrov, A. A., Ochkov, A. V. & Ochkov, V. F. WaterSteamPro documentation www.wsp.ru (2021).
27. Stapmanns, J. et al. Thermal critical points and quantum critical end point in the frustrated bilayer Heisenberg antiferromagnet. *Phys. Rev. Lett*. **121**, 127201 (2018).
28. Kageyama, H. et al. Exact dimer ground state and quantized magnetization plateaus in the two-dimensional spin system $SrCu_2(BO_3)_2$. *Phys. Rev. Lett*. **82**, 3168–3171 (1999).
29. Larrea J, J., Martelli, V. & Rønnow, H. M. High-pressure specific heat technique to uncover novel states of quantum matter. *J. Phys. Conf. Ser*. **1609**, 012008 (2020).
30. Boos, C. et al. Competition between intermediate plaquette phases in $SrCu_2(BO_3)_2$. *Phys. Rev. B* **100**, 140413 (2019).
31. Nojiri, H., Kageyama, H., Onizuka, K., Ueda, Y. & Motokawa, M. Direct observation of the multiple spin gap excitations in two-dimensional dimer system $SrCu_2(BO_3)_2$. *J. Phys. Soc. Jpn*. **68**, 2906–2909 (1999).
32. Fisher, M. E. & Upton, P. J. Universality and interfaces at critical end points. *Phys. Rev. Lett*. **65**, 2402 (1990).
33. Fisher, M. E. & Barbosa, M. C. Phase boundaries near critical end points. I. Thermodynamics and universality. *Phys. Rev. B* **43**, 11177–11184 (1991).
34. Bettler, S., Stoppel, L., Yan, Z., Gvasaliya, S. & Zhedulev, Z. Competition between intermediate plaquette phases in $SrCu_2(BO_3)_2$. *Phys. Rev. Res*. **2**, 012010 (2020).
35. Lee, J. Y., You, Y.-Z., Sachdev, S. & Vishwanath, A. Signatures of a deconfined phase transition on the Shastry–Sutherland lattice: applications to quantum critical $SrCu_2(BO_3)_2$. *Phys. Rev. X* **9**, 041037 (2019).
36. Waki, T. et al. A novel ordered phase in $SrCu_2(BO_3)_2$ under high pressure. *J. Phys. Soc. Jpn*. **76**, 073710 (2007).
37. Maxim, F. et al. Visualization of supercritical water pseudo-boiling at Widom line crossover. *Nat. Commun*. **10**, 4114 (2019).
38. Sordi, G., Haule, K. & Tremblay, A.-M. S. Finite doping signatures of the Mott transition in the two-dimensional Hubbard model. *Phys. Rev. Lett*. **104**, 226402 (2010).
39. Terletska, H., Vučičević, J., Tanasković, D. & Dobrosavljević, V. Quantum critical transport near the Mott transition. *Phys. Rev. Lett*. **107**, 026401 (2011).
40. Eisenlohr, H., Lee, S.-S. B. & Vojta, M. Mott quantum criticality in the one-band Hubbard model: dynamical mean-field theory, power-law spectra, and scaling. *Phys. Rev. B* **100**, 155152 (2019).
41. Furukawa, T., Miyagawa, K., Taniguchi, H., Kato, R. & Kanoda, K. Quantum criticality of Mott transition in organic materials. *Nat. Phys*. **11**, 221–224 (2015).

Methods

Samples

Single crystals of $SrCu_2(BO_3)_2$ were grown by a floating-zone method. First, polycrystalline $SrCu_2(BO_3)_2$ was prepared by a solid-state reaction using as starting materials $SrCO_3$, CuO and B_2O_3 with 99.99% purity. These were mixed, ground and heat-treated at 900 °C in flowing oxygen for over 100 h with several intermediate grindings. The phase purity was verified by conventional X-ray diffractometry and the powder was pressed hydrostatically into rods (8 mm in diameter and around 90 mm in length) which were sintered at 900 °C for 20 h in an oxygen atmosphere.

Single-crystal growth was carried out using an optical floating zone furnace (FZ-T-10000-H-IV-VP-PC, Crystal Systems) with four 300-W halogen lamps as the heat source. Although the first reported single crystals of $SrCu_2(BO_3)_2$ were also grown in this type of furnace, using $LiBO_2$ discs as a solvent placed on a top of a seed rod[42], we obtained better results using a self-adjusted flux method[43]. Optimal growth conditions were found to be a steady growth rate of 0.25 mm h^{-1} at all times, rotation of both feeding and seeding rods at approximately 15 rpm in opposite directions to ensure homogeneity of the liquid and the application of a 5-bar pressure of argon with 20% oxygen. When a homogeneous melt was achieved, the power of the lamps was decreased slowly (over 24 h) until steady-state conditions were found (approximately 48.5% lamp power in the present case), after which these conditions were maintained rigorously until the end of the growth. The full growth process required approximately two weeks and resulted in a recrystallized boule 8 cm in length containing a single-crystalline grain in its top 4 cm.

Specific-heat measurements

Three slabs were cut from the single-crystal rod, each with a cross-section of 7.6–9.0 mm^2 in the *ab* plane and a thickness of 0.5–1.0 mm parallel to the *c* axis. The sample masses were measured to be between 15 and 36 mg. The samples were polished gently to deposit Pt films of 20-nm thickness. To measure the heat capacity, $C(P, H, T)$, under multiple extreme conditions (very low temperatures, high pressures and intense magnetic fields), we used a.c. calorimetry at a second-harmonic mode (2ω). We employed a piston cylinder BeCu clamp cell to apply pressures up to 26.5 kbar, with liquid kerosene as the pressure-transmitting medium. Measurements of the electrical resistivity at the superconducting transition of a Pb strip were used as a pressure manometer and revealed good hydrostatic conditions in our experiments. The pressure cell was inserted into a cryostat with a ^{3}He–^{4}He dilution refrigerator that enabled both cell and sample to be cooled to 0.1 K with temperature variations below 1 mK. At some pressure steps, a magnetic field up to 9 T was applied using a superconducting magnet the field direction of which was parallel to the *c* axis.

Our a.c. calorimetry set-up was sputtered onto the sample slab to guarantee good thermal contact of the sample, heater and thermometer[29]. It consisted of two separate Pt films, one used as the heater and the other used to improve the thermal contact between sample and thermometer, as shown in Extended Data Fig. 1a. This configuration enabled the efficient measurement of the modulated temperature difference in the sample (ΔT_{ac}) as a function of the amplitude and frequency, $f = \omega/(2\pi)$, of the alternating excitation current, $I_{ex} = I_0 e^{-i\omega t}$. The heating power was applied through two Constantan wires (H_{1a} and H_{1b} in Extended Data Fig. 1a), this choice of metal being made to avoid heat leakage through the wires; the gold wires (H_{2a} and H_{2b}) were applied to measure the electrical resistance of the heater as a function of *P*, *H* and *T*. We used a AuFe(0.07)/Chromel thermocouple (TC_2 in Extended Data Fig. 1a) as the thermometer detecting the temperature differential, ΔT_{ac}, between the sample and its environment, and placed a second thermocouple (TC_1) symmetrically opposite to it; because TC_1 showed the same *f* dependence of ΔT_{ac} as did TC_2, we could conclude that there were no thermal gradients across the sample within the resolution of our experiment.

The sample heat capacity was obtained directly from the isothermal *f* scans, shown in Extended Data Fig. 1b, c, by fitting with the standard steady-state equation[44]. Given the complete control of all relevant a.c. calorimetry parameters, our method has a number of advantages in the determination of absolute values of $C(P, H, T)$ when compared with previous work[19]. These advantages include a more precise determination of the corrections for unwanted heat losses throughout the sample, a more precise separation of additional *P*-dependent contributions and the ability to achieve an optimal thermal equilibrium inside the sample (within the resolution of the thermocouple). Thus, our '*f*-scan' analysis[29] allows an accurate determination of the working frequency (f_C) at which to maximize $C(P, H, T)$ at each pressure. Extended Data Fig. 1c, d demonstrates the correct determination of $f_C = 1.5$ Hz at $P = 18.2$ kbar, whose measurement at fixed f_C (a '*T* scan') reproduces the same result as obtained from our *f*-scan analysis[29].

For practical purposes in our measurements of $SrCu_3(BO_2)$, we found that the range of pressures and fields covered by our current investigation had negligible influence on the relevant parameters in the steady-state equation. Thus we measured the *T* dependence of the heat capacity of each sample at a constant field and at a fixed frequency, f_C, determined for each pressure. Our methodology allowed us to determine the heat capacity within an accuracy of 5% with respect to an adiabatic technique. Further details concerning all aspects of the procedures of our a.c. calorimetry measurements may be found in previous work[29].

Fully frustrated bilayer

The Heisenberg model on the fully frustrated bilayer[27] presents a clear, and thus conceptually valuable, example of a first-order QPT giving rise to a critical point at finite temperature. In this geometry, which has no known materials analogue, spin pairs (with coupling $J_\perp$) are arranged vertically on a square lattice with equal couplings ($J_\parallel$) to both spins of all four dimer neighbours, and the ground state jumps discontinuously from exact dimer singlets to exact triplets at $J_\perp/J_\parallel = 2.315$. With increasing temperature, the discontinuity in triplet density reduces until the line of first-order transitions terminates at a critical point, in the 2D Ising universality class, when $k_B T_c \approx 0.52 J_\parallel$ (ref. [27]). The geometry of the fully frustrated bilayer has a direct connection to that of the Shastry–Sutherland model[45], suggesting that the two may share similar critical-point physics. A discontinuity in the average dimer spin–spin correlation is certainly well documented at the dimer–plaquette QPT in the Shastry–Sutherland model. However, the models do differ in that the total spin of each dimer is a good quantum number in the fully frustrated bilayer, but not in the Shastry–Sutherland case. A further point of contrast is that the QPT of the fully frustrated bilayer is from the dimer-singlet phase to a 2D antiferromagnetic phase, which by the Mermin–Wagner theorem has no finite-temperature transition, forcing the critical point associated with the discontinuity to be observed as an isolated point. The fact that the plaquette phase of the Shastry–Sutherland model has a thermal Ising transition raises in principle the alternative scenario of the tricritical point, which we show is excluded by our experimental and numerical results.

iPEPS

Tensor-network methods provide a powerful approach for accurate numerical calculations of both the ground and thermal states of gapped local Hamiltonians. iPEPS[20,21,46], a 2D generalization of matrix-product states, are a variational ansatz enabling both wavefunctions and thermal states[22,47–50] to be represented efficiently in the thermodynamic limit, with the accuracy of the representation controlled systematically by the bond dimension, *D*, of the tensors.

To obtain an iPEPS representation of a thermal state, we employ the algorithms used previously[22], which are based on the imaginary-time

evolution of a purification of the thermal density operator. At each time step the bond dimension of the iPEPS is truncated to the maximal D. To maximize D while working near the QPT, we restrict the truncation to the (local) simple-update approach[17,51]. To improve the efficiency of the calculations, we exploit the global U(1) symmetry of the model[52,53], which for a pure Heisenberg model is preserved in the presence of an applied field at finite temperatures. Physical expectation values are computed by contracting the tensor network, which we perform by a development[54] of the corner-transfer-matrix method[55,56].

This method is also used to compute the transfer matrix, from which we extract the correlation length, ξ in Fig. 1d and Extended Data Fig. 3b, of the correlation function with the slowest decay. iPEPS with a sufficiently large but finite D can be used to represent a critical state at finite temperature, as in the early example of the 2D Ising model[55]. In the Shastry–Sutherland model we have found that $D = 8$ is already large enough to obtain a diverging ξ on approaching the critical point, as we show in Extended Data Fig. 2; we remark that the region of parameter space over which the divergence is visible is considerably narrower than the point spacing of 0.001 shown in Fig. 1 and Extended Data Fig. 3.

In the Shastry–Sutherland problem, the optimal tensor geometry depends on the ground state[14]: the spin correlations of the dimer phase are represented most efficiently using one tensor per dimer in a two-dimer unit cell[17], whereas correlations in the plaquette phase are best described by an ansatz with one tensor per four sites (from four different dimers) on a plaquette[14]. For working around a critical point, it is essential to use a single representation of both quantum phases, and in the Shastry–Sutherland model the plaquette basis is more efficient for representing the dimer phase than the reverse. For this reason, we have used the plaquette basis for all of the results reported here.

As a consequence we do observe numerical instabilities at the lowest temperatures when working in the dimer phase (the regions excluded from Figs. 1c–e, 2c, d). These are most probably an artefact arising because of the product nature of the dimer ground state, as all observables and energies are essentially converged at those temperatures. One means of circumventing this problem is to add a small Dzyaloshinskii–Moriya interaction to the model, in fact guided by the real spin Hamiltonian of $SrCu_3(BO_2)_2$. This leads to an entangled ground state, which, as shown in Extended Data Fig. 3, makes the low-temperature regime accessible, albeit at cost of a reduced D. These results confirm further that the Dzyaloshinskii–Moriya interactions of $SrCu_3(BO_2)_2$ have no effect on the physics of the critical point.

When working in the plaquette phase, the strongly entangled nature of the plaquette ground state makes low-temperature studies very challenging, and for this reason our primary focus is on temperatures $T/J_D \gtrsim 0.03$, for a full characterization of the regime relevant to the critical point. Although a small feature is evident in C/T around $T/J_D = 0.02$ (Extended Data Fig. 3a), we caution against associating this with the Ising transition of the plaquette phase, because we do not find corresponding behaviour in the spin correlations and thus cannot confirm the reliability of our results at such low temperatures.

Data availability

The data that support the findings of this study are available at https://doi.org/10.5281/zenodo.4455613 and from the corresponding author upon reasonable request.

Code availability

The code that supports the findings of this study is available from the corresponding author upon reasonable request.

42. Kageyama, H., Onizuka, K., Yamauchi, T. & Ueda, Y. Crystal growth of the two-dimensional spin gap system $SrCu_3(BO_2)_2$. *J. Cryst. Growth* **206**, 65–67 (1999).
43. Jorge, G. A. et al. High magnetic field magnetization and specific heat of the 2D spin–dimer system $SrCu_2(BO_3)_2$. *J. Alloys Compd.* **369**, 90–92 (2004).
44. Gmelin, E. Classical temperature-modulated calorimetry: a review. *Thermochim. Acta* **304–305**, 1–26 (1997).
45. Wessel, S. et al. Thermodynamic properties of the Shastry–Sutherland model from quantum Monte Carlo simulations. *Phys. Rev. B* **98**, 174432 (2018).
46. Nishio, Y., Maeshima, N., Gendiar, A. & Nishino, T. Tensor product variational formulation for quantum systems. Preprint at https://arxiv.org/abs/cond-mat/0401115 (2004).
47. Li, W. et al. Linearized tensor renormalization group algorithm for the calculation of thermodynamic properties of quantum lattice models. *Phys. Rev. Lett.* **106**, 127202 (2011).
48. Czarnik, P., Cincio, L. & Dziarmaga, J. Projected entangled pair states at finite temperature: imaginary time evolution with ancillas. *Phys. Rev. B* **86**, 245101 (2012).
49. Czarnik, P. & Dziarmaga, J. Projected entangled pair states at finite temperature: iterative self-consistent bond renormalization for exact imaginary time evolution. *Phys. Rev. B* **92**, 035120 (2015).
50. Kshetrimayum, A., Rizzi, M., Eisert, J. & Orús, R. Tensor network annealing algorithm for two-dimensional thermal states. *Phys. Rev. Lett.* **122**, 070502 (2019).
51. Jiang, H. C., Weng, Z. Y. & Xiang, T. Accurate determination of tensor network state of quantum lattice models in two dimensions. *Phys. Rev. Lett.* **101**, 090603 (2008).
52. Singh, S., Pfeifer, R. N. C. & Vidal, G. Tensor network states and algorithms in the presence of a global U(1) symmetry. *Phys. Rev. B* **83**, 115125 (2011).
53. Bauer, B., Corboz, P., Orús, R. & Troyer, M. Implementing global Abelian symmetries in projected entangled-pair state algorithms. *Phys. Rev. B* **83**, 125106 (2011).
54. Corboz, P., Rice, T. M. & Troyer, M. Competing states in the *t–J* model: uniform *d*-wave state versus stripe state. *Phys. Rev. Lett.* **113**, 046402 (2014).
55. Nishino, T. & Okunishi, K. Corner transfer matrix renormalization group method. *J. Phys. Soc. Jpn.* **65**, 891–894 (1996).
56. Orús, R. & Vidal, G. Simulation of two-dimensional quantum systems on an infinite lattice revisited: corner transfer matrix for tensor contraction. *Phys. Rev. B* **80**, 094403 (2009).
57. Luo, J., Xu, L., Stanley, H. E. & Buldyrev, S. V. Behavior of the Widom line in critical phenomena. *Phys. Rev. Lett.* **112**, 135701 (2014).

Acknowledgements We are grateful to R. Gaal, J. Piatek and M. de Vries for technical assistance. We acknowledge discussions with D. Badrtdinov, C. Boos, T. Fennell, A. Sandvik, A.-M. Tremblay, A. Turrini, A. Wietek and A. Zheludev. We thank the São Paulo Research Foundation (FAPESP) for financial support under grant no. 2018/08845-3, the Qatar Foundation for support through Carnegie Mellon University in Qatar's Seed Research programme, the Swiss National Science Foundation (SNSF) for support under grant no. 188648 and the European Research Council (ERC) for support under the EU Horizon 2020 research and innovation programme (grant no. 677061), as well as from the ERC Synergy Grant HERO. We are grateful to the Deutsche Forschungsgemeinschaft for the support of RTG 1995 and to the IT Center at RWTH Aachen University and the JSC Jülich for access to computing time through JARA-HPC. The statements made herein are not the responsibility of the Qatar Foundation.

Author contributions The experimental project was conceived by H.M.R. and Ch.R. and the theoretical framework was put forward by F.M. The crystals were grown by E.P. and K.C. Specific-heat measurements were performed by J.L.J. with assistance from M.E.Z., R.L. and H.M.R. S.P.G.C. and P.C. performed iPEPS calculations. A.M.L. performed complementary exact diagonalization calculations. L.W. and S.W. performed quantum Monte Carlo simulations on the fully frustrated bilayer model. Data analysis and figure preparation were performed by J.L.J., E.F., S.P.G.C., L.W., S.W., P.C. and H.M.R. The detailed theoretical analysis was provided by P.C., S.P.G.C., F.M., A.H., B.N., L.W. and S.W. The manuscript was written by B.N. and F.M. with assistance from all the authors.

Competing interests The authors declare no competing interests.

Additional information
Supplementary information The online version contains supplementary material available at https://doi.org/10.1038/s41586-021-03411-8.

Correspondence and requests for materials should be addressed to H.M.R.

Peer review information *Nature* thanks Jong Yeon Lee and the other, anonymous, reviewer(s) for their contribution to the peer review of this work. Peer reviewer reports are available.

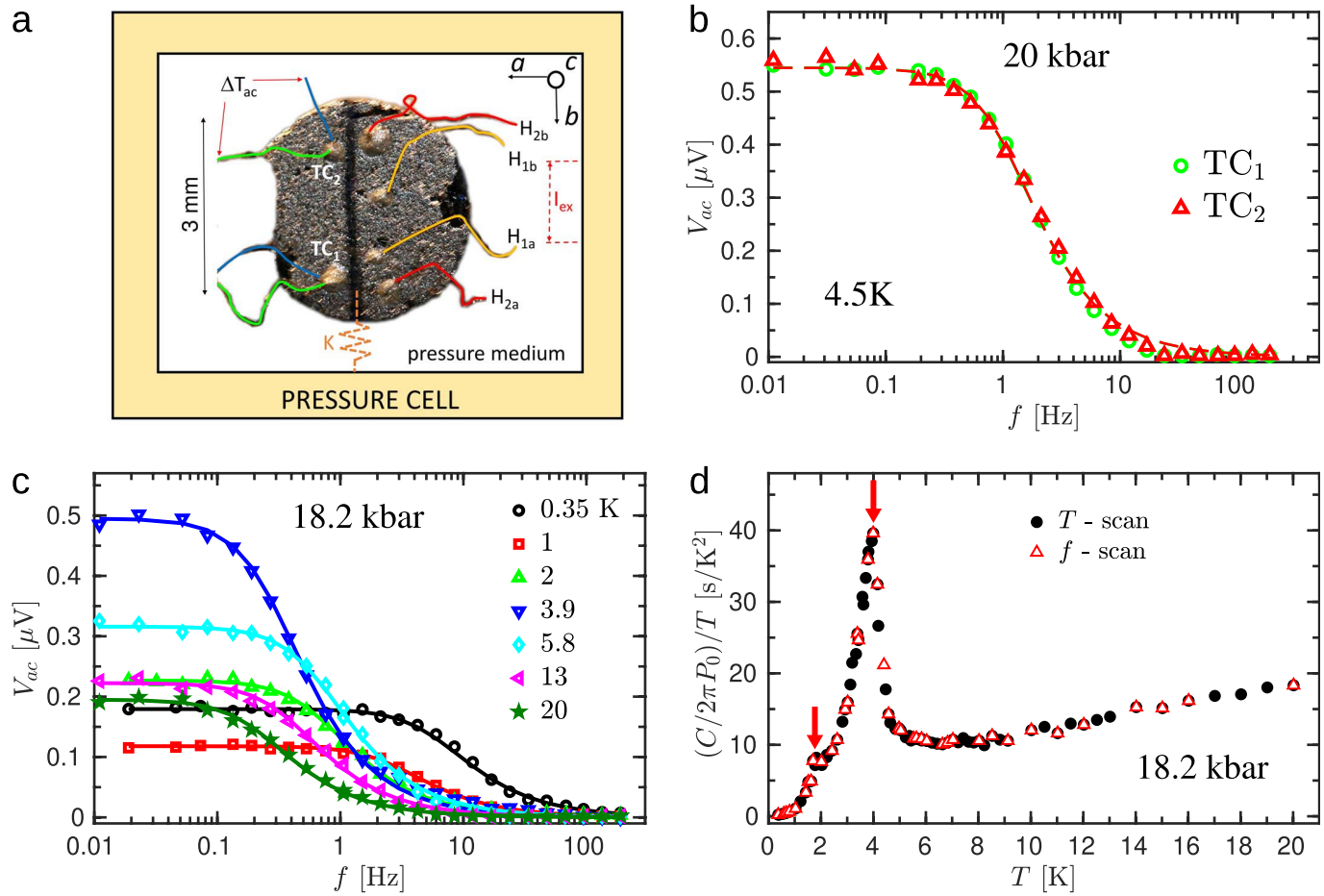

Extended Data Fig. 1 | a.c. calorimetry on $SrCu_2(BO_3)_2$. a, The a.c. calorimeter was prepared by depositing two Pt thin films (the shinier surfaces) over both halves of the sample. One film was used as the heater and the other for optimal thermal contact and measurement. The heating current (I_{ex} at frequency f) was supplied through the pair of Constantan wires labelled H_{1a} and H_{1b}, and H_{2a} and H_{2b} were used to measure the electrical resistance, R_{Pt}, of the Pt film. TC_1 and TC_2 are thermocouples and K represents the thermal contact between the sample and the cryostat (through the pressure cell). **b**, Isothermal ($T = 4.5$ K) and isobaric ($P = 20$ kbar) f dependence of the modulated pick-up voltage, V_{ac}, which is directly proportional to the temperature differential, ΔT_{ac}, measured by the thermocouples at two different positions. **c**, Isobaric ($P = 18.2$ kbar) f-dependence measurements of V_{ac} at different temperatures with $I_0 = 1.6$ mA at $T \geq 3.9$ K, $I_0 = 0.8$ mA at $T = 2$ K and $I_0 = 0.4$ mA at $T < 2$ K. **d**, Sample heat capacity normalized to the input heating power ($P_0 = I_0^2 R_{Pt}$), comparing the fit of $V_{ac}(f)$ obtained from the steady-state equation ('f scan')[29] with values obtained directly from a variable-temperature measurement performed at the fixed working frequency $f_c = 1.5$ Hz ('T scan'). Solid and dashed lines in **b** and **c** represent fits using the steady-state equation[29,44].

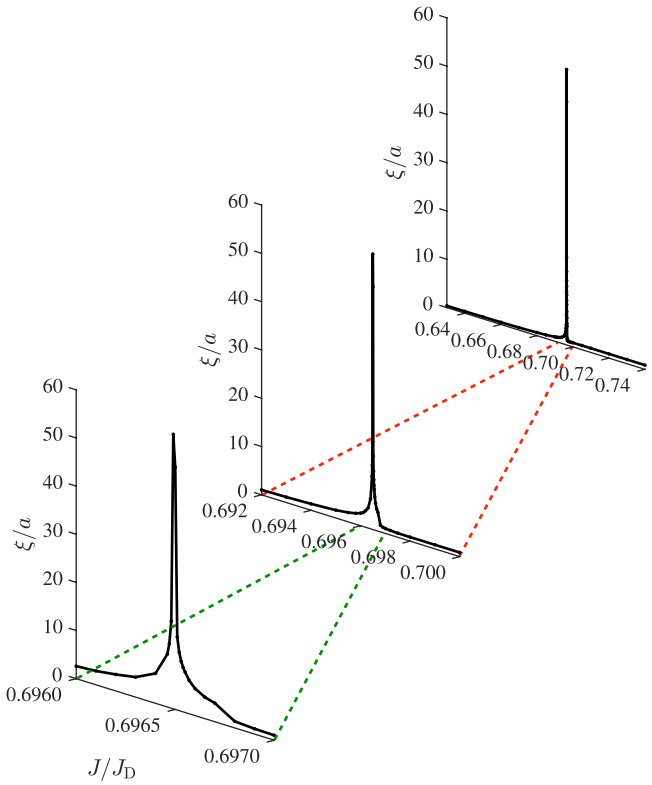

Extended Data Fig. 2 | Correlation length. ξ/a for the Shastry–Sutherland model, calculated by iPEPS with $D = 8$ as a function of the coupling ratio, J/J_D, at a fixed temperature $T_c(D = 8) = 0.0522 J_D/k_B$. The three panels show increasing magnification of the J/J_D axis from the equivalent of Fig. 1 (upper right) through the step sizes of Fig. 2c, d ($10^{-3} J/J_D$, centre) to $10^{-5} J/J_D$ (lower left).

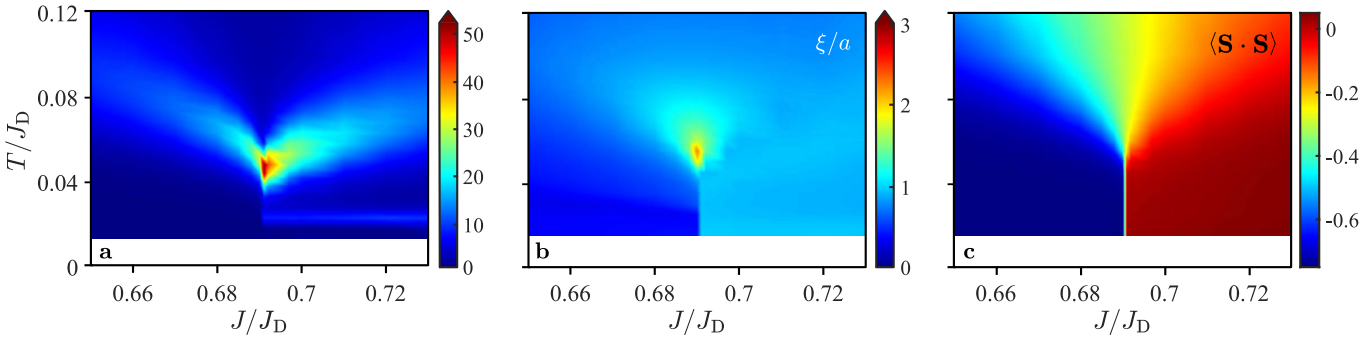

Extended Data Fig. 3 | Critical point in the presence of Dzyaloshinskii–Moriya interactions. Thermodynamic data obtained from iPEPS calculations with $D = 10$ performed for the Shastry–Sutherland model in the presence of Dzyaloshinskii–Moriya interactions. These interactions, of strength D_D, are placed on the dimer (J_D) bonds and have the magnitude known for $SrCu_2(BO_3)_2$. They create an entangled ground state in the dimer phase, which resolves the numerical instabilities observed for the pure Shastry–Sutherland model at low temperatures, although the reduced symmetry limits the maximum D to 10. **a**, Specific heat, $C(J/J_D, T)/T$, shown in the same format as for Fig. 1b, c. **b**, Correlation length, ξ/a, showing clearly the region of 'pressure' and temperature over which Ising correlations develop. **c**, Dimer spin–spin correlation function, $\langle \mathbf{S}_i \cdot \mathbf{S}_j \rangle$, emphasizing the abrupt onset with decreasing temperature of a sharp discontinuity as a function of J/J_D. It is clear that these Dzyaloshinskii–Moriya interactions have no qualitative effect whatsoever on the physics of the critical point.

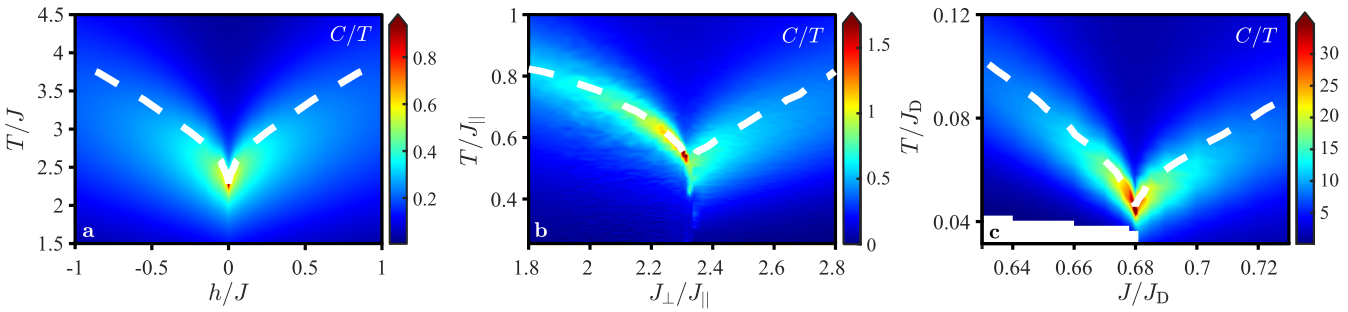

Extended Data Fig. 4 | Ising critical points in different lattice models. Specific heat, C/T, for a number of 2D models, illustrating its universal behaviour around the Ising critical point. **a**, Ising model on the square lattice in a longitudinal magnetic field, h, obtained by contracting the exact $D = 2$ tensor-network representation of the partition function using the corner-transfer-matrix method with a boundary bond dimension $\chi = 24$ (ref. [55]). **b**, Fully frustrated bilayer model, obtained by using the stochastic series expansion quantum Monte Carlo approach developed in refs. [27,45] to perform simulations on systems of sizes up to $2 \times 32 \times 32$ as a function of $J_\perp/J_\parallel$. **c**, Shastry–Sutherland model, obtained by iPEPS calculations with $D = 20$ as in Fig. 1c. The dashed lines show the positions of the local maxima of the specific heat, $C(J/J_D)$, which we label by their temperatures, T_{max}. These two lines reach an absolute minimum, $T_{max} = T_c$, where they meet at the Ising critical point, with T_{max} increasing as the control parameter is changed away from the QPT. Thus the specific heat defines two characteristic lines in the phase diagram of the Ising critical point, instead of the single line given by the correlation length (Fig. 1d) and the critical isochore (Fig. 1e). This contrasting behaviour has been demonstrated in models where the critical pressure is temperature-independent[57] and the issue of characteristic lines has also been discussed in the Mott metal–insulator phase diagram[38,40]. We stress that such behaviour is a fundamental property of the Ising model, and hence of all models sharing its physics. For the Shastry–Sutherland model (**c**), the two lines of maxima can be taken to provide a qualitative definition of regimes dominated by 'dimer-like' spin correlations (lower left) and by 'plaquette-like' correlations (lower right, but above the plaquette-ordered phase), accompanied by a third regime (above both lines) bearing no clear hallmarks of either $T = 0$ phase. We remark that the values of T_c in units of the relevant energy scale, $T_c/J \approx 2.3$ (**a**), $T_c/J \approx 0.53$ (**b**) and $T_c/J \approx 0.04$ (**c**), vary widely among the three models. This can be traced to the change in slope of the ground-state energy at the transition, the compensation of which by entropy effects restores a derivable free energy at T_c.